Catalysis Science & Technology

ROYAL SOCIETY OF CHEMISTRY

PAPER

View Article Online
View Journal | View Issue

Cite this: *Catal. Sci. Technol.*, 2020, **10**, 2029

A mechanistic study of microstructure modulation in olefin polymerizations using a redox-active Ni(II) α-diimine catalyst†

Robert C. Chapleski Jr., [a] Jesse L. Kern, ‡[b] W. Curtis Anderson Jr., ‡[a] Brian K. Long [a] and Sharani Roy *[a]

Polyolefins are among the world's most widely produced and utilized classes of polymers, serving as synthetic alternatives to traditional materials such as wood, glass, and metal. While numerous prior research efforts have focused on the development of faster, more efficient, and less expensive catalysts, recent studies have demonstrated that redox-active olefin polymerization catalysts may also be employed to modulate catalytic activity, reactivity, and selectivity *in situ*. One example of these efforts is the modulation of polyolefin microstructure and comonomer incorporation *via* the use of a redox-switchable Ni(II) α-diimine catalyst. Though this capability is intriguing, neither the mechanisms that lead to this behavior nor the structures of the active reduced catalyst species are completely understood. Herein, we report a computational study based on density functional theory designed to better understand the structure and underlying olefin polymerization mechanisms of the active catalytic species in two distinct redox states. These findings are further supported through experimental evidence and suggest that upon activation of the reduced catalyst species, the added electron density of the catalyst is transferred from the active metal center to the α-diimine ligand. Consequently, the observed decrease in polyethylene branching that results from catalyst reduction is believed to stem from changes in the subtle balance of steric, electronic, and entropic effects, primarily perturbing the coordination of subsequent monomer units. This perturbation is expressed not only in the monomer-inserted-product energy differences but also in the catalysts' deviation from square planarity about the Ni center. Through these studies, we can better understand how the addition of an electron to a Ni(II) α-diimine catalyst perturbs its catalytic behavior, which may influence the design of future generations of redox-active olefin polymerization catalysts.

Received 16th December 2019,
Accepted 16th January 2020

DOI: 10.1039/c9cy02538c

rsc.li/catalysis

Introduction

Advances in late-transition-metal olefin polymerization catalysts have enabled the synthesis of polyolefins with varying microstructures using a limited number of monomeric feedstocks.[1–10] Because of the industrial importance of polyolefins, it is imperative that researchers develop a deep fundamental understanding of how structural and/or electronic modifications of a given ligand/catalyst system influence the microstructure of a resultant polyolefin. Through such studies, we may gain insight into catalytic structure–property relationships and enable the development of catalysts with precise and/or tailored polymerization control.

One particular methodology that has garnered significant attention due to its unique ability to facilitate catalytic control, is the use of redox-active catalysts.[11–23] Redox-active catalysts are species that undergo oxidation or reduction at the active metal center or its surrounding ligand. This change

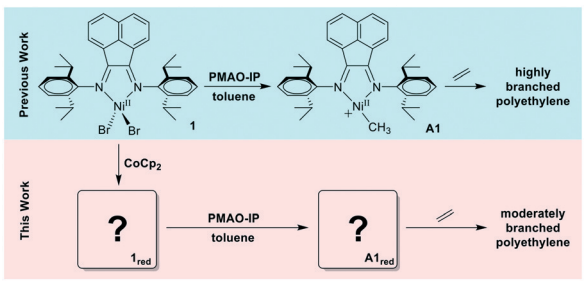

Fig. 1 Investigation of the modulation of polyethylene microstructure by redox-active olefin polymerization catalyst **1**.

[a] *Department of Chemistry, University of Tennessee, Knoxville, TN 37996, USA*
[b] *Department of Chemistry, Randolph College, Lynchburg, VA 24503, USA.*
E-mail: sharani.roy@utk.edu

† Electronic supplementary information (ESI) available: Computational details, catalyst dimerization pathways, partial molecular-orbital diagrams, experimental details, annotated NMRs, atomic coordinates of calculated catalysts, reactants, intermediates, and transition states (*XYZ*). See DOI: 10.1039/c9cy02538c

‡ These authors contributed equally.

in oxidation state perturbs the electronic environment at the catalytically active center and may alter the rates of initiation, propagation, chain transfer, and termination processes. Recently, independent reports by Chen and Long demonstrated the first examples of redox-active olefin polymerization catalysts, which used either a ferrocenyl-substituted Pd-based catalyst or α-diimine-ligated Ni catalyst, respectively.[14,21]

Of particular interest to this study, the Ni-based α-diimine precatalyst, (1,2-bis[(2,6-diisopropylphenyl)imino]-acenaphthene)$NiBr_2$, or dipp-BIAN$NiBr_2$, (**1**), was recently shown to be a competent redox-active catalyst,[21] which is capable of producing multiple polyethylene (PE) microstructures as a function of added reductant (Fig. 1). Therein, Long and coworkers showed that the branching content of PE produced by **1** could be decreased by >20% when one equivalent of the reducing agent cobaltocene ($CoCp_2$) was added to **1** before activation by methylaluminoxane (MAO) and subsequent addition of ethylene. In a related study, they demonstrated that the relative uptake of hexene in ethylene–hexene copolymerizations using precatalyst **1** was decreased when one equivalent of cobaltocene was added to **1** prior to the addition of MAO and monomers.[24] Therefore, it has been shown that microstructures of both PE and ethylene–hexene copolymers can be effectively modulated by switching the redox state of precatalyst **1**.

The redox activity of **1** was proposed to arise due to the ability of the α-diimine, or 1,2-bis(arylimino)-acenaphthene (BIAN), ligand, to accept an electron from the added chemical reductant. This hypothesis was based upon the knowledge that BIAN-type ligands have been shown to facilitate multiple reductions, up to the −4 oxidation state, due to their extended π-backbone and diimine structure.[25,26] Furthermore, these redox-active ligands have been used for a variety of other redox-active complexes that employ metal centers such as Ni,[27] Mg,[28] Ca,[26] Zn,[29] Ga,[30] Al,[31] and Co.[32]

Based upon EPR evidence, it was proposed that reduction of precatalyst **1** using cobaltocene initially reduces the Ni(II) center to Ni(I), but that this added electron is then transferred to the BIAN ligand upon methylation and activation by MAO.[21] It was also noted that adding trimethylaluminum (TMA), a common contaminant in MAO, also appears to facilitate metal-to-ligand electron transfer, but that the resulting system was inactive for polymerization unless MAO was added. This observation is supported by the work of Gao and co-workers, who also proposed reduction of the Ni center prior to intramolecular electron transfer to the BIAN ligand.[27]

The current understanding of the structure and function of redox-active precatalyst **1** is depicted in Fig. 1, in which the MAO-activated form of the precatalyst, labeled as **A1**, is generally considered to be well understood.[1,6,33–36] However, as highlighted by Fig. 1, there remain a number of significant questions such as: (1) what is the structure of precatalyst $\mathbf{1_{red}}$, [dipp-BIAN$NiBr_2$]$^-$, which is formed by the treatment of precatalyst **1** with cobaltocene? (henceforth, the subscript "red" in a label indicates that the species results from the reduced precatalyst). (2) What is the structure of the MAO-activated form of the reduced catalyst ($\mathbf{A1_{red}}$)? Lastly, (3) what chemical and mechanistic differences between **A1** and $\mathbf{A1_{red}}$ give rise to the observed microstructural differences in ethylene homopolymerization and ethylene–hexene copolymerization?

In this paper, we address these questions through a systematic computational study based on density functional theory (DFT) that is compared to previously reported and new experimental evidence. As a note, previous computational studies of precatalyst **1** have used QM/MM methods to investigate the non-reduced form of the catalyst. Specifically, Woo and Ziegler[37] studied the effect of different backbone substituents on ethylene capture using a QM/MM method comprised of the BP86 functional and an augmented AMBER95 force field. More recently, Meneghetti and coworkers[38] studied polymer growth up to the pentyl chain using a QM/MM method comprised of the B3LYP functional and the Universal force field (UFF). Herein, we extend these studies to now consider the reduced form of the catalyst **1** using a fully quantum-mechanical approach. Based on these computational studies and supported by experimental evidence, we are able to offer a potential explanation as to how a change in the redox state of this Ni(II) α-diimine catalyst is able to produce varying polymer microstructures in both ethylene homopolymerizations and ethylene–hexene copolymerizations. Similar computational studies have been conducted for other redox-active systems.[39–43]

Methods

General experimental methods and materials

All reactions were performed under an inert nitrogen atmosphere using an MBraun UniLab glovebox or using standard Schlenk techniques, unless otherwise noted. All solvents were dried using an Innovative Technologies PureSolv solvent purification system and degassed *via* three freeze–pump–thaw cycles. Precatalyst **1** was prepared according to literature.[2] CD_2Cl_2 was dried over activated molecular sieves (4 Å) and degassed by three freeze–pump–thaw cycles prior to use. PMAO-IP was obtained from Akzo Nobel as a 2.3 M solution in toluene and used as received. All other reagents were purchased from commercial vendors and used without further purification. Polyethylene ^{1}H spectra were recorded at 20 °C using a Varian 500 MHz NMR spectrometer in $CDCl_3$ or using a Bruker 400 MHz NMR spectrometer in $C_2D_2Cl_4$. Evans method experiments were performed according to literature procedures.[44] EPR measurements were obtained using a Bruker EMX (X-band) EPR spectrometer. The MATLAB package EasySpin was used to generate simulated EPR spectra.

General polymerization procedure

To a Fisher–Porter bottle was added precatalyst **1** (10 μmol) dissolved in dichloromethane (DCM) (2 mL), toluene (50

mL), and a magnetic stir bar. The bottle was sealed and placed in a water bath at the desired temperature. The vessel was pressurized with ethylene (75 psi) and allowed to equilibrate under constant pressure for 10 min with stirring. Either trimethylaluminum (TMA) solution (1.0 M in toluene) or PMAO-IP (2.3 M in toluene) was injected to initiate polymerization and was stirred continuously for the desired time. The polymerization was quenched by addition of MeOH (10 mL) and the polymer was precipitated by adding excess acidic MeOH (5% HCl in MeOH). The polymer was stirred in acidic methanol overnight before being filtered and dried in a vacuum oven to constant weight.

Polymerizations requiring the reduced catalyst form were performed using identical conditions, except cobaltocene (10 μmol, 1 equiv.) was added to the precatalyst **1**/DCM solution prior to PMAO-IP injection.

Computational methods

The computational study was performed using DFT within the Gaussian09 quantum-chemistry software package.[45] Precatalyst **1** has a total of 81 atoms, including 5 atoms heavier than carbon, and a total of 368 electrons. All electrons of the catalysts, reactants, reactive intermediates, and transition states were treated explicitly in the calculations. The TPSSh exchange–correlation functional[46] was used in conjunction with the Dunning cc-pVTZ basis set.[47,48] TPSSh was chosen due to its accurate description of geometric and electronic properties of precatalysts **1** and $\mathbf{1_{red}}$, as well as its overall good performance for organometallic complexes.[49–60] Further, TPSSh has recently been shown to be effective in estimating the contribution of metal atoms to frontier molecular orbitals[61] in redox-switching systems[62] as well as predicting hyperfine coupling constants integral to EPR spectra.[63] The functional was corrected for dispersion using Grimme's D3 empirical dispersion scheme[64] with Becke–Johnson damping parameters.[65] Precatalyst $\mathbf{1_{red}}$ was modeled by adding an electron to precatalyst **1**. Similarly, the MAO-activated form of $\mathbf{1_{red}}$ (*i.e.*, $\mathbf{A1_{red}}$) was modeled by adding an electron to the proposed MAO-activated form of **1** (**A1**). All calculations were performed in the presence of a solvent environment of toluene, described using the implicit polarizable continuum model (PCM).[66] The stability of wavefunctions was checked and corrected when necessary. Free energies of all species were calculated at 298 K. Barring two structures in Fig. S5 of the ESI,† all calculated vibrational frequencies of catalysts, reactants, and reactive intermediates reported in this work are real, and each transition state contains a single imaginary vibrational frequency along the reaction coordinate. The evaluation and validation of the functional, basis set, integration grid, and solvent model are presented in the ESI.†

Results and discussion

Our study is comprised of four parts. First, we calculate the geometries and spin densities of precatalysts **1** and $\mathbf{1_{red}}$, and compare our results to measured EPR spectra of the two species. Second, we model the activation of precatalysts **1** and $\mathbf{1_{red}}$ by MAO and propose structures of the catalytically active forms, **A1** and $\mathbf{A1_{red}}$. In the third and fourth parts of the study, we use these active forms to model the mechanistic pathways that lead to differentiation between **1** and $\mathbf{1_{red}}$ for ethylene homopolymerization and ethylene–hexene copolymerization.

Characterization of precatalysts 1 and $\mathbf{1_{red}}$

Reduction of precatalyst **1** with 1 equivalent of cobaltocene yields precatalyst $\mathbf{1_{red}}$ as previously reported.[21] Fig. 2 shows the molecular structures, DFT-optimized geometries, and spin densities of precatalysts **1** and $\mathbf{1_{red}}$. These results suggest that both **1** and $\mathbf{1_{red}}$ are tetrahedral complexes that differ in one critical way: while precatalyst **1** contains Ni in an oxidation state of +2, precatalyst $\mathbf{1_{red}}$ contains Ni in an oxidation state of +1. This indicates a formal reduction at the metal center rather than the ligand itself, and also agrees with previous experimental findings.[21,27] The spin density, *i.e.* unpaired-electron density, of **1** is concentrated in the d orbitals of Ni, indicating a d^8 triplet spin-state of the metal center, while the spin density of $\mathbf{1_{red}}$ is also concentrated on Ni, indicating a d^9 doublet spin-state of the metal center.

This change in Ni oxidation state upon catalyst reduction affects the immediate geometric environment of the metal center, as detailed in the ESI† (Fig. S6 and S7). The Ni–N and Ni–Br bond lengths of complex **1** were calculated to be 2.03 Å and 2.35 Å, respectively, and 1.99 Å and 2.40 Å, respectively, for complex $\mathbf{1_{red}}$. Furthermore, the N–Ni–N, Br–Ni–Br, and Br–Ni–N bond angles were calculated to be 82.9°, 130.6°, and 108.3°, respectively, for complex **1**, and 82.8°, 108.8°, and 110.4°, respectively for complex $\mathbf{1_{red}}$. The computed structure of **1** could not be directly compared to its known crystal structure as precatalyst **1** exists as a dimer in the solid, crystal state. However, the calculated geometry at the Ni center

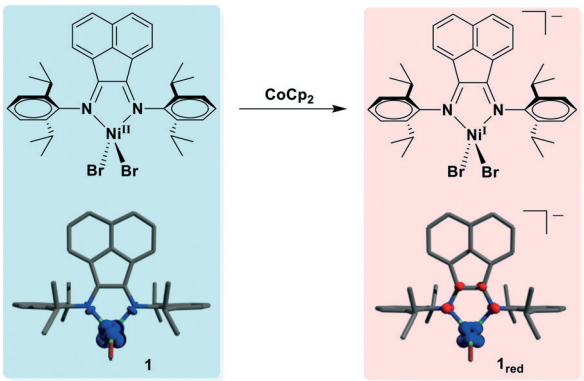

Fig. 2 DFT-optimized geometries and spin densities of precatalysts **1** (left pane) and $\mathbf{1_{red}}$ (right pane). Mulliken spin densities ($\alpha > \beta$, blue; $\alpha < \beta$, red) are shown with an isosurface of 0.015 electrons per $Bohr^3$ for metal-centered spin densities. Atom colors are: C = grey; N = blue; Ni = green; Br = red. Hydrogen atoms are omitted for clarity.

compares well to that of crystal structures of related catalysts, as shown in the ESI† (Table S2).

As previously described, when precatalyst $\mathbf{1}_{red}$ is activated by MAO (resulting in $\mathbf{A1}_{red}$), the polyethylene product displays significantly decreased branching content in comparison to polymers made using **A1**.[21] Before computing the catalytic pathways of **A1** and $\mathbf{A1}_{red}$ to investigate the mechanistic rationale behind this behavior, it was necessary to verify that the calculated electronic states of **1** and $\mathbf{1}_{red}$ correctly describe their corresponding redox states. Magnetic susceptibility measurements were performed following the Evans method revealing that complex **1** displays a magnetic susceptibility of $3.2\mu_B$, which suggests a tetrahedral Ni(II) center with two unpaired electrons,[21] and that is in agreement with calculated results. This complex was also found to be EPR-silent, corroborating the calculated triplet spin state of the metal center.[21] Magnetic susceptibility measurements of reduced complex $\mathbf{1}_{red}$ revealed a magnetic susceptibility of $2.5\mu_B$, strongly supporting the presence of a Ni(I) center with only one unpaired electron,[21] also in agreement with calculated results. The EPR spectrum of $\mathbf{1}_{red}$ measured in toluene (Fig. 3) exhibits a signal at g = 2.32 at 77 K and at g = 2.35 at 298 K, both of which indicate the reduction of the Ni(II)-center to yield Ni(I).[21] Our DFT-calculated g-value of 2.31 for reduced precatalyst $\mathbf{1}_{red}$ is in good agreement with experiment, providing strong evidence that $\mathbf{1}_{red}$ indeed exists as a metal-centered radical formed following treatment of **1** with cobaltocene.

The magnetic susceptibility measurements and EPR spectra provide key evidence that the calculated species **1** and $\mathbf{1}_{red}$, wherein **1** has undergone a one-electron reduction at Ni to form $\mathbf{1}_{red}$, correctly represent the unreduced and reduced precatalysts, respectively. However, one could also envision that the reduction of precatalyst **1** might lead to other different, yet related species. Therefore, we computationally investigated the potential process in which the addition of an electron to precatalyst **1** dissociates one of the Ni–Br bonds, subsequently forming an overall neutral, solvent-coordinated species. This species could then dimerize to produce a different form of the reduced catalyst, as shown in the ESI.† As a note, these reduced structures are Ni(I) species, and therefore could potentially give rise to the observed g-value of 2.32 in its experimental EPR spectrum. Several α-diimine-ligated Ni(I) complexes have been previously reported in the literature; however, the exact role of those species in the polymerization has yet to be understood.[10,27,67–71] Based on our DFT-calculated free-energy pathway (ESI,† Fig. S5), we conclude that $\mathbf{1}_{red}$ (Fig. 2) is the most stable form of the reduced catalyst and will be used for computations throughout the remainder of this work.

Activation of precatalysts 1 and $\mathbf{1}_{red}$ by MAO

The activation of precatalyst **1** by MAO is believed to occur *via* a series of halide abstractions and methylations. This process ultimately yields a Ni(II) species with a single methyl group and open coordination site to which ethylene or other olefinic monomer can coordinate.[1,6,33] The currently accepted structure of activated precatalyst **1** (*i.e.*, **A1**) is shown in Fig. 1, and though we have drawn this species with a fully open coordination site, it is also likely that this species may exist either as an activator-bound or solvent-bound complex. The polymerization reaction begins when an ethylene molecule coordinates to the now-activated Ni(II) center of **A1** and undergoes migratory insertion into the Ni–C bond of the bound methyl group. To examine the electronic nature of **A1**, and to determine whether the analogous reduced active species $\mathbf{A1}_{red}$ is in fact structurally or energetically distinct

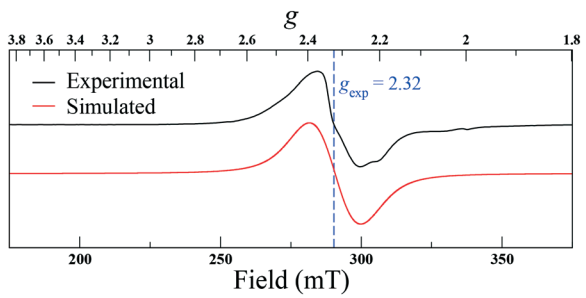

Fig. 3 Experimental EPR spectrum (black) of complex $\mathbf{1}_{red}$ in toluene at 77 K, and the corresponding EasySpin fit (red) reveal a transition at g = 2.32, which is indicative of a metal-centered radical. This g-value strongly suggests that reduction of **1** by cobaltocene results in the formation of a Ni(I) species.

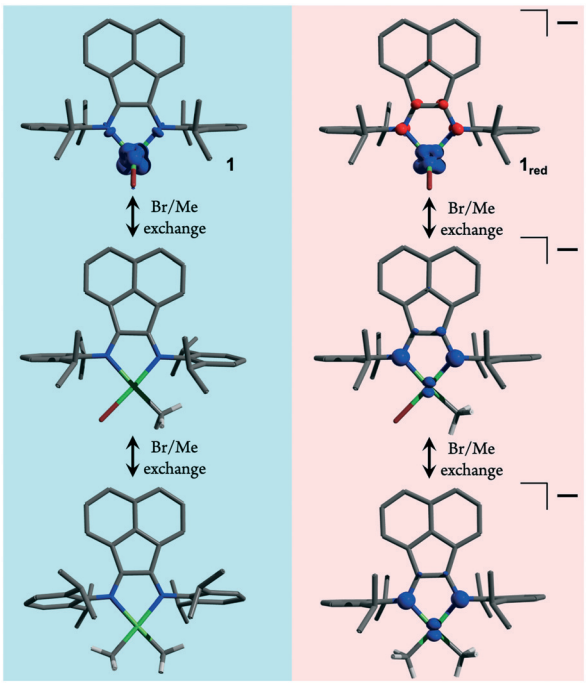

Fig. 4 DFT-optimized geometries and spin densities at successive stages of methylation of **1** and $\mathbf{1}_{red}$. Mulliken spin densities ($\alpha > \beta$, blue; $\alpha < \beta$, red) are shown with an isosurface of 0.015 electrons per Bohr^3. Colors of atoms are the same as in Fig. 2. Non-methyl hydrogen atoms are omitted for clarity, and methyl hydrogens are shown in white.

from **A1**, we computationally studied both the methylation and methyl-abstraction steps of the activation of **1** and $\mathbf{1_{red}}$ by MAO.

Fig. 4 shows the DFT-optimized geometries and spin densities for **1** and $\mathbf{1_{red}}$ as the bromide ligands are successively substituted by methyl groups. Results show that methylation switches the geometry of both **1** and $\mathbf{1_{red}}$ from tetrahedral to square-planar. As the geometry of precatalyst **1** changes to square-planar, the +2 oxidation state of Ni is retained, but the spin state of the Ni(II) center changes from triplet to singlet, as demonstrated by the spin density going to zero. In contrast, as the geometry of precatalyst $\mathbf{1_{red}}$ changes to square planar, the added electron in $\mathbf{1_{red}}$ might be expected to remain localized on the Ni(I) center by occupying the high energy $d_{x^2-y^2}$ orbital; however, spin densities obtained from DFT calculations show that this is not the case. Instead, a significant fraction of the electron density is transferred from Ni to the dipp-BIAN ligand, transforming the reduced catalyst from a metal-centered radical to a primarily ligand-centered radical. The ratio of spin densities of Ni : dipp-BIAN changes from 2.48 in $\mathbf{1_{red}}$ to 0.28 upon substitution of the bromide ligands by methyl ligands. These results demonstrate that methylation has the same geometric effect but different electronic effects on the active Ni centers of **1** and $\mathbf{1_{red}}$. While the oxidation state of Ni in **1** remains at +2 upon activation/methylation, the Ni center of complex $\mathbf{1_{red}}$ is re-oxidized from +1 to +2.

We tested this computational result by experimentally measuring the EPR spectrum of $\mathbf{1_{red}}$ treated with five equivalents of the methylating agent TMA. As observed in Fig. 5, methylation of $\mathbf{1_{red}}$ changes its room-temperature EPR *g* value from 2.31 to 2.006, strongly indicating the presence of an organic ligand-based radical that results from the transfer of the added electron from the Ni center to the aromatic dipp-BIAN ligand upon methylation and concomitant geometry change to square-planar.[21]

Fig. 6 shows the DFT-optimized geometries and spin densities for active species **A1** and $\mathbf{A1_{red}}$, which were obtained by abstraction of one methyl group and subsequent coordination of an explicit toluene solvent molecule. The key

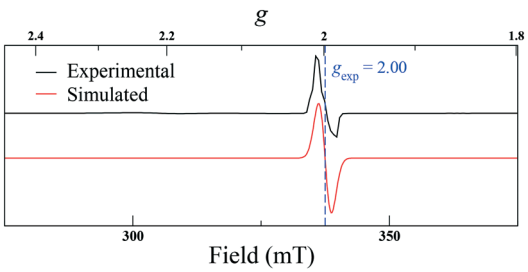

Fig. 5 Experimental EPR spectrum (black) of complex $\mathbf{1_{red}}$ in toluene at room temperature treated with five equivalents of TMA., and the corresponding EasySpin fit (red) reveal a transition at g = 2.00, which is indicative of a ligand-centered radical. This *g*-value strongly suggests that reduction and methylation of **1** by TMA results in the formation of a Ni(II) species.

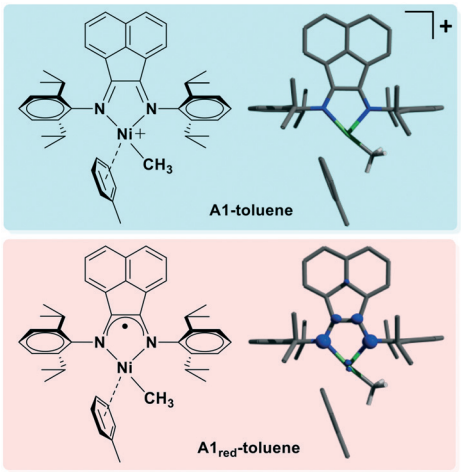

Fig. 6 DFT-optimized structures of proposed catalytically active species **A1** formed from **1**, and $\mathbf{A1_{red}}$ formed from $\mathbf{1_{red}}$. Colors of atoms and Mulliken spin densities of **A1** (spin singlet) and $\mathbf{A1_{red}}$ (spin doublet) are shown as in Fig. 4.

difference between these species is that **A1** features a cationic Ni center, whereas $\mathbf{A1_{red}}$ is neutral. We note that, with such a neutral charge, $\mathbf{A1_{red}}$ is not expected to be coordinated to a cobaltocenium counterion. Both active metal centers are in the +2 oxidation state and retain the square-planar geometries formed during methylation.

Consequently, **A1** has zero spin density, whereas reduced species $\mathbf{A1_{red}}$ clearly shows that its added electron is primarily delocalized on the N–C–C–N fragment of the dipp-BIAN ligand, with a small fraction on Ni (Fig. 6). The ratio of spin densities of Ni : dipp-BIAN in $\mathbf{A1_{red}}$ is 0.05. This primary delocalization of the added electron density on the ligand agrees well with the calculated *g*-value of $\mathbf{A1_{red}}$, which was found to be 2.01, and that is in good agreement with the experimental *g*-value of 2.006 for $\mathbf{1_{red}}$ + TMA. Furthermore, though the additional electron in $\mathbf{A1_{red}}$ primarily resides on the ligand, the slight additional electron density on Ni modulates the electronic nature of the metal center by reducing its electrophilicity. This indirect electronic effect was also observed by Kim and coworkers, who synthesized a series of sterically and electronically modulated α-diimine ligands and classified the electrophilicity of their Ni(II) complexes by cyclic voltammetry.[72] The effects of the reduced electrophilicity of $\mathbf{A1_{red}}$ on polymerization are described in the following two sections.

Ethylene capture and polymer branching by precatalysts 1 and $\mathbf{1_{red}}$

The catalytic polymerization of ethylene by **1** and $\mathbf{1_{red}}$ follows a coordination–insertion polymerization mechanism, as shown in Scheme 1. First, ethylene binds to the catalytically active species (**A1** or $\mathbf{A1_{red}}$), which then undergoes migratory insertion into the nearby Ni–carbon bond to extend the growing polymer chain. These two steps can continuously

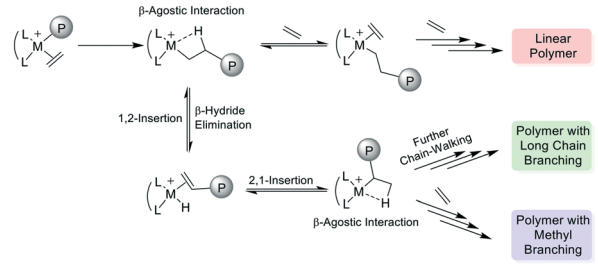

Scheme 1 Coordination polymerization mechanism.

repeat to form a linear polymer chain until a chain termination step occurs. However, branching may occur along the polymer chain through a competitive process known as chain-walking.

Chain-walking occurs when the propagating metal center undergoes β-hydride elimination followed by 2,1-insertion of the coordinated olefin into the metal-hydride. This process may happen one or more times prior to subsequent ethylene coordination and insertion, thereby leading to polyethylenes containing methyl or longer-chain branches, respectively (Scheme 1). To understand how reduction of catalyst **1** decreases branching of polyethylene, we have examined the ethylene coordination, migratory insertion, β-hydride elimination, and 2,1-insertion steps for **A1** and $\mathbf{A1_{red}}$. As a note, the active species was modeled with an open coordination site in this portion of our study.

In order to understand the mechanistic differences between MAO-activated polymerization using catalysts **A1** and $\mathbf{A1_{red}}$, we first present experimental results for the two cases. Table 1 shows that polymerizations using **A1** (**1**/MAO) (entries 1 and 2) produces polyethylene with a branching content of 98 branches/1000 carbon atoms. In contrast, polymerizations using the reduced catalyst system $\mathbf{A1_{red}}$ (**1**/$CoCp_2$/MAO) result in a similar polyethylene yields but with a decreased branch content of 66 branches/1000 carbon atoms (Table 1, entries 3 and 4). This more than 30% decrease in polymer branching when using the reduced-catalyst system $\mathbf{1_{red}}$/MAO system suggests that the chain-walking process is considerably suppressed in $\mathbf{A1_{red}}$ as compared to **A1**, which we hypothesized is due to the lower electrophilicity of the Ni atom in the reduced active species.

Fig. 7 shows our DFT-computed free-energy diagram for the binding of ethylene to **A1** (blue trace) and $\mathbf{A1_{red}}$ (red trace), followed by ethylene insertion to form an *n*-propyl group, and subsequent binding of a second ethylene molecule to the open coordination site. Results show that ethylene binds more weakly to $\mathbf{A1_{red}}$ (ΔG_{bind} = −10.9 kcal mol^{-1}) than to **A1** (ΔG_{bind} = −18.2 kcal mol^{-1}). This provides evidence that the electrophilicity of $\mathbf{A1_{red}}$ is indeed lower than that of **A1**. The migratory insertion of this ethylene to form an *n*-propyl chain (see Fig. 7) is more favorable for **A1** ($\Delta G_{insertion}$ = −7.1 kcal mol^{-1}) than for $\mathbf{A1_{red}}$ ($\Delta G_{insertion}$ = −5.1 kcal mol^{-1}) due to the stronger β-agostic interaction[73] between Ni and an *n*-propyl β-hydrogen at the open-coordination site of **A1** compared to $\mathbf{A1_{red}}$. Again, this is likely due to the more electrophilic nature of Ni in **A1** (and $\mathbf{I\text{-}1^{n\text{-}pr}}$) than in $\mathbf{A1_{red}}$ (and $\mathbf{(I\text{-}1^{n\text{-}pr})_{red}}$). As calculated from a natural-bond-order analysis,[74] a decrease in the atomic charge of the Ni atom upon reduction supports the decreased electrophilicity of the reduced system (+0.782 |e| for **A1** and +0.769 |e| for $\mathbf{A1_{red}}$; +0.499 |e| for $\mathbf{I\text{-}1^{n\text{-}pr}}$ and +0.457 |e| for **(I-**

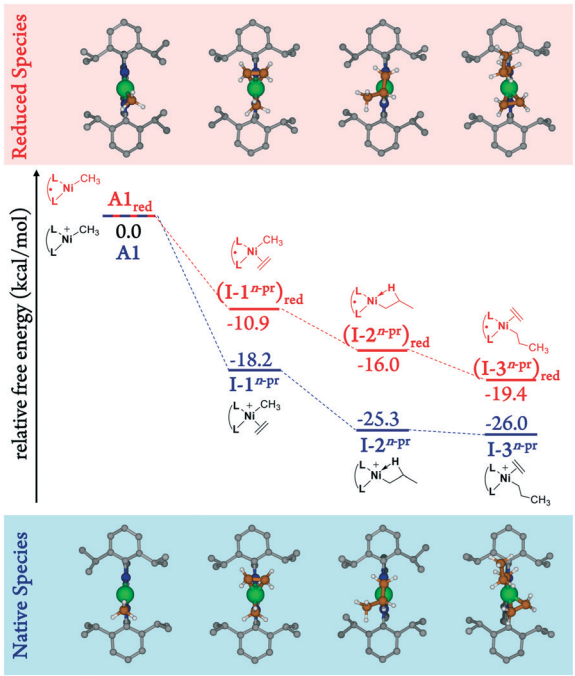

Fig. 7 Free energy profile in kcal mol^{-1} of the initial ethylene binding, migratory insertion, and second-ethylene binding steps of polymer growth using **A1** (blue) and $\mathbf{A1_{red}}$ (red). For ball-and-stick structures of stationary points, atom colors are the same as in Fig. 2, with the additional highlighting of propyl and ethylene carbons in brown. Hydrogen atoms on the dipp-BIAN ligand are omitted for clarity.

Table 1 Polymer characterization for the 1/MAO and 1/$CoCp_2$/MAO reactions

Entry	Catalytic system	Yield (g)	Branches/1000 C[c]	Ref.
1[a]	**1**/MAO	1.75	114	Previous work[21]
2[b]	**1**/MAO	2.9	98	This work
3[a]	**1**/$CoCp_2$/MAO	1.78	88	Previous work[21]
4[b]	**1**/$CoCp_2$/MAO	2.5	66	This work

[a] Polymerization conditions: [1] = 10.0 μmol, 148 mL of toluene, 2 mL of DCM, 20 °C, 15 psi ethylene, 30 min, and 92 equiv. of PMAO-IP. [b] Polymerization conditions: [1] = 10.0 μmol, 48 mL of toluene, 2 mL of DCM, 20 °C, 75 psi ethylene, 15 min, and 500 equiv. of MAO. [c] Branches per 1000 total carbon atoms determined by ^{1}H NMR.

$\mathbf{1}^{n\text{-pr}})_{red}$). As a result of the stronger β-agostic interaction in **I-2**$^{n\text{-pr}}$ as compared to $(\mathbf{I\text{-}2}^{n\text{-pr}})_{red}$, the coordination of a second ethylene is less favorable to **I-2**$^{n\text{-pr}}$ (ΔG_{bind} = −0.7 kcal mol^{-1}) relative to $(\mathbf{I\text{-}2}^{n\text{-pr}})_{red}$ (ΔG_{bind} = −3.4 kcal mol^{-1}). Excluding thermochemical corrections, our calculated second-ethylene binding energy of ΔE_{bind} = −14.1 kcal mol^{-1} for **A1** compares well with results of QM/MM calculations performed by Woo and Ziegler, who calculated a second-ethylene binding energy of ΔE_{bind} = −14.0 kcal mol^{-1} for **A1** when fully considering steric and electronic effects.[37]

To further investigate the differences in the catalytic mechanism between **A1** and $\mathbf{A1}_{red}$, DFT calculations were performed to study the isomerization of the *n*-propyl ligand, which leads to a linear polymer, to an iso-propyl ligand, which leads to a polymer branch, prior to the second ethylene coordination. Fig. 8 compares the free-energy pathways for isomerization of the propyl ligand in complex **I-2**$^{n\text{-pr}}$ (**A1**-derived pathway) to isomerization of the propyl ligand in complex $(\mathbf{I\text{-}2}^{n\text{-pr}})_{red}$ ($\mathbf{A1}_{red}$-derived pathway), followed by binding of a second ethylene molecule. Free energies are plotted relative to the π-propylene coordinated Ni(II) hydride α-diimine complex (**I-4**) and its reduced analogue ($(\mathbf{I\text{-}4})_{red}$), which are each formed following β-hydride elimination of intermediates **I-2**$^{n\text{-pr}}$ or $(\mathbf{I\text{-}2}^{n\text{-pr}})_{red}$, respectively. The reaction pathways leading to the iso-propyl (branched) species are shown on the left, whereas reaction pathways leading to the *n*-propyl (linear) species are shown on the right of Fig. 8.

The right side of Fig. 8 shows that complex **I-4** (or $(\mathbf{I\text{-}4})_{red}$ in the case of $\mathbf{A1}_{red}$) can undergo 1,2-insertion to produce the *n*-propyl-ligated species **I-2**$^{n\text{-pr}}$ (or $(\mathbf{I\text{-}2}^{n\text{-pr}})_{red}$ in the case of $\mathbf{A1}_{red}$) followed by coordination by ethylene to form species **I-3**$^{n\text{-pr}}$ (or $(\mathbf{I\text{-}3}^{n\text{-pr}})_{red}$ in the case of $\mathbf{A1}_{red}$). Alternatively, complex **I-4** or $(\mathbf{I\text{-}4})_{red}$ can undergo 2,1-insertion to form an iso-propyl ligand **I-2**$^{i\text{-pr}}$ or $(\mathbf{I\text{-}2}^{i\text{-pr}})_{red}$ followed by coordination of ethylene to produce complex **I-3**$^{i\text{-pr}}$ or $(\mathbf{I\text{-}3}^{i\text{-pr}})_{red}$, which is shown on the left side of the pathway.

Results show that the difference between free energies of activation for addition of the hydrogen atom to C_2 *versus* C_1 of the bound propylene monomer are similar for **I-4** ($\Delta\Delta G^{\ddagger}$ = 2.7–1.3 = 1.4 kcal mol^{-1}) and $(\mathbf{I\text{-}4})_{red}$ ($\Delta\Delta G^{\ddagger}$ = 5.4–3.8 = 1.6 kcal). Further, the difference between free energies of activation for second-ethylene addition to **I-2**$^{i\text{-pr}}$ *versus* to **I-2**$^{n\text{-pr}}$ ($\Delta\Delta G^{\ddagger}$ = 12.8–9.5 = 3.3 kcal mol^{-1}) is similar to the analogous difference between $(\mathbf{I\text{-}2}^{i\text{-pr}})_{red}$ and $(\mathbf{I\text{-}2}^{n\text{-pr}})_{red}$ ($\Delta\Delta G^{\ddagger}$ = 15.4–11.7 = 3.7 kcal mol^{-1}). However, whereas the free energy of complex **I-3**$^{n\text{-pr}}$ is lower than that of **I-3**$^{i\text{-pr}}$ by 0.9

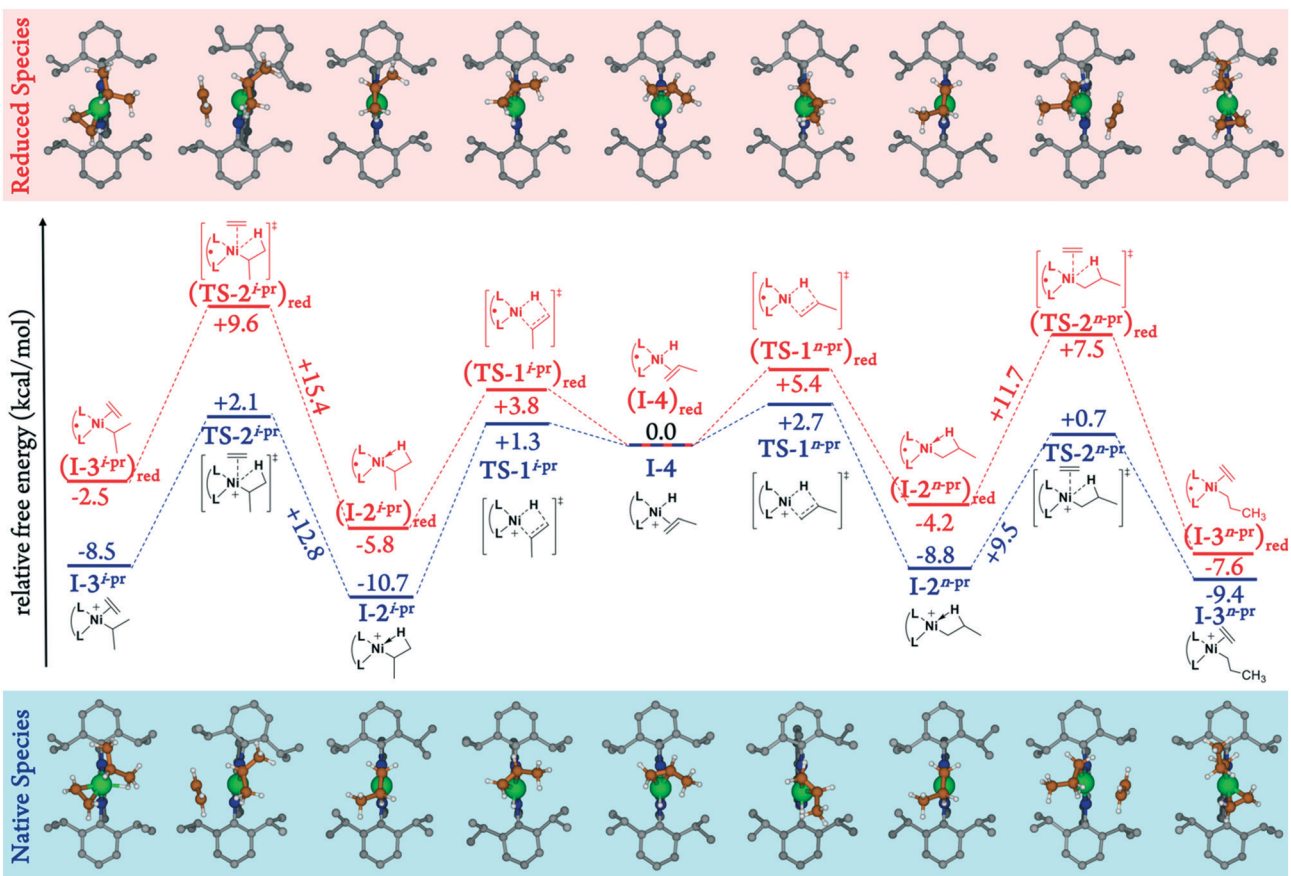

Fig. 8 Structures and relative free energies of intermediates and transition states in the catalytic reaction pathway to isomerize the propyl group and bind the second ethylene molecule during polymerization. Free energies are reported in kcal mol^{-1} and set relative to complex **I-4** for the **A1**-derived pathway (blue) and complex $(\mathbf{I\text{-}4})_{red}$ for the $\mathbf{A1}_{red}$-derived pathway (red). TS indicates a transition state. Same color scheme for ball-and-stick structures as in Fig. 7.

kcal mol^{-1}, the free energy of complex **(I-3$^{n\text{-pr}}$)$_{red}$** is lower than that of **(I-3$^{i\text{-pr}}$)$_{red}$** by 5.1 kcal mol^{-1}. Based upon this data, we can conclude that the difference in the branching content of PE obtained from the reduced *versus* non-reduced forms of the catalyst arises primarily from thermodynamic, rather than kinetic, differences in the calculated reaction pathways.

The thermodynamic preference for a less-branched polymer in the reduced system as shown by the difference in free energies of **(I-3$^{n\text{-pr}}$)$_{red}$** and **(I-3$^{i\text{-pr}}$)$_{red}$**, compared to the analogous difference between **I-3$^{n\text{-pr}}$** and **I-3$^{i\text{-pr}}$**, arises from a competitive interplay between steric and electronic effects in these intermediate species. To understand this interplay, we examined the square planarity of these complexes by defining a planar angle between the N–Ni–N plane and the plane containing the C═C$_{ethylene}$ bond center, the Ni atom, and the C atom of the propyl substituent that is bound to Ni. According to this convention, a square-planar complex would have a planar angle of 0°, whereas a tetrahedral complex would have a planar angle of 90°.

Our calculations revealed that complex **I-3$^{n\text{-pr}}$** has a planar angle of 23°, whereas complex **I-3$^{i\text{-pr}}$** has a planar angle of 49°, indicating a stronger steric repulsion between the iso-propyl ligand and the dipp-BIAN ligand relative to the *n*-propyl ligand. In the isomerization pathway derived from **A1$_{red}$** (Fig. 8), the added electron density residing primarily on the dipp-BIAN ligand makes it a more strongly donating ligand, thereby increasing the ligand-field splitting of the d orbitals of Ni(II) (ESI,† Fig. S8 and S9), and consequently increasing the square planarity of both **(I-3$^{n\text{-pr}}$)$_{red}$** (planar angle = 6°) and **(I-3$^{i\text{-pr}}$)$_{red}$** (planar angle = 37°). However, the greater steric repulsion between the iso-propyl group and diisopropylphenyl group destabilizes its free energy relative to that of **(I-3$^{n\text{-pr}}$)$_{red}$** by 5.1 kcal mol^{-1}.

Despite a planar-angle difference of 26° between **I-3$^{i\text{-pr}}$** and **I-3$^{n\text{-pr}}$**, the difference in free energies of the two complexes is only 0.9 kcal mol^{-1} due to a favorable agostic interaction between the β-hydrogen of the iso-propyl branch with the Ni center in **I-3$^{i\text{-pr}}$**. Such a β-agostic interaction does not form in **(I-3$^{i\text{-pr}}$)$_{red}$** due to the reduced electrophilicity of Ni, and does not form in either **I-3$^{n\text{-pr}}$** or **(I-3$^{n\text{-pr}}$)$_{red}$** due to the longer distance between the β-hydrogen atom and the Ni center. DFT-optimized geometries, interatomic distances, and atomic charges related to the β-agostic interaction are shown in Fig. S11–S13 and Tables S4–S6 (see ESI†). Consequently, in the **A1**-derived pathway, the additional β-agostic interaction compensates for distortion from square planarity and steric repulsion in **I-3$^{i\text{-pr}}$**, making it energetically very close to **I-3$^{n\text{-pr}}$**. The loss of the favorable β-agostic interaction in the **A1$_{red}$**-derived pathway due to the lower electrophilicity of Ni creates a larger free-energy gap between **(I-3$^{i\text{-pr}}$)$_{red}$** and **(I-3$^{n\text{-pr}}$)$_{red}$** and decreases branching in the polyethylene product.

Ethylene–hexene copolymerization by precatalysts 1 and 1$_{red}$

Previous reports have shown that copolymerizations of ethylene and 1-hexene using the reduced catalyst **A1$_{red}$** consume less 1-hexene than identical copolymerizations performed using **A1**, albeit with virtually identical ethylene consumption.[24] To understand the reasoning for this differentiation in 1-hexene consumption upon reduction of catalyst **1**, we computationally compared the coordination of ethylene *versus* hexene to the propyl-ligated complex **I-2$^{n\text{-pr}}$** in the **A1**-derived pathway, as well as to complex **(I-2$^{n\text{-pr}}$)$_{red}$** in the **A1$_{red}$**-derived pathway.

Fig. 9 shows a free-energy diagram for the binding of an ethylene molecule to **I-2$^{n\text{-pr}}$** to form **I-3$^{n\text{-pr}}$** (left pathway), or a hexene molecule to **I-2$^{n\text{-pr}}$** to form **I-5$^{n\text{-pr}}$** (right pathway), as well as the corresponding **A1$_{red}$**-derived pathways. Complex **I-5$^{n\text{-pr}}$** has approximately the same free energy as complex **I-2$^{n\text{-pr}}$**, whereas the free energy of activation to bind hexene to **I-2$^{n\text{-pr}}$** ($\Delta G^{\ddagger}$ = 6.8 kcal mol^{-1}) is lower than the free energy of activation to bind ethylene to **I-2$^{n\text{-pr}}$** ($\Delta G^{\ddagger}$ = 9.4 kcal mol^{-1}). In contrast, the **A1$_{red}$**-derived pathway shows that the free energy of **(I-3$^{n\text{-pr}}$)$_{red}$** is lower than that of **(I-5$^{n\text{-pr}}$)$_{red}$** by 1.7 kcal mol^{-1}. The free energy of activation to bind hexene ($\Delta G^{\ddagger}$ = 11.2 kcal mol^{-1}) to **(I-2$^{n\text{-pr}}$)$_{red}$** is notably similar to the free energy of activation to bind ethylene ($\Delta G^{\ddagger}$ = 11.7 kcal mol^{-1}). Therefore, the consumption of hexene in ethylene–hexene copolymerization is decreased both thermodynamically and kinetically by reduction of precatalyst **1** to precatalyst **1$_{red}$**.

A decomposition of the free-energy gap between **(I-5$^{n\text{-pr}}$)$_{red}$** and **(I-3$^{n\text{-pr}}$)$_{red}$** (ΔG = 1.7 kcal mol^{-1}) into its enthalpic (ΔH = −1.6 kcal mol^{-1}) and entropic components ($T\Delta S$ = −3.3 kcal

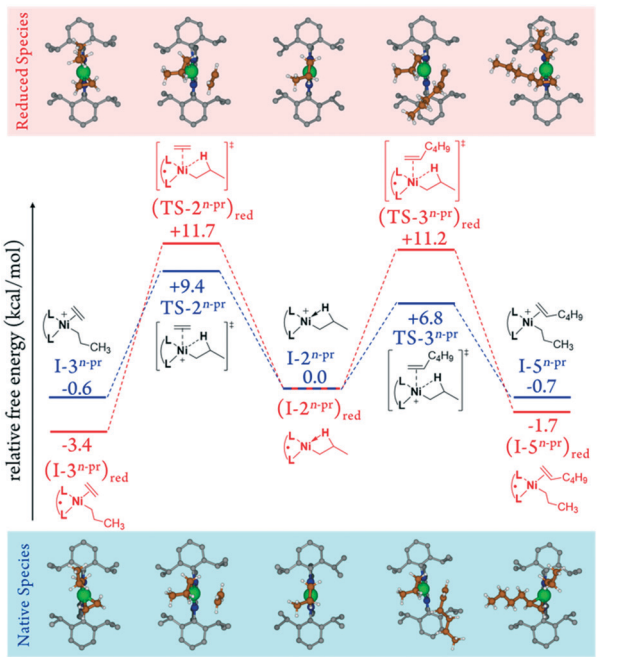

Fig. 9 Structures and relative free energies of intermediates and transition states for ethylene binding *versus* hexene binding in the catalytic copolymerization of ethylene and hexene. Free energies are reported in kcal mol^{-1} and set relative to complex **I-2$^{n\text{-pr}}$** for the **A1**-derived pathway (blue) and complex **(I-2$^{n\text{-pr}}$)$_{red}$** for the **A1$_{red}$**-derived pathway (red). TS indicates a transition state. Same color scheme for ball-and-stick structures as in Fig. 7.

mol^{-1}) (at room temperature, Table S7†) reveals that the free-energy difference results primarily from a larger entropic penalty of binding hexene compared to ethylene upon catalyst reduction. In contrast, the free-energy gap of ΔG = 5.1 kcal mol^{-1} between $(\mathbf{I\text{-}3^{i\text{-}pr}})_{\mathbf{red}}$ and $(\mathbf{I\text{-}3^{n\text{-}pr}})_{\mathbf{red}}$ (Fig. 8, Table S7†) results primarily from an enthalpic difference of ΔH = 3.2 kcal mol^{-1}, compared to an entropic contribution of −1.9 kcal mol^{-1}. Thus, whereas steric repulsion and breaking of β-agostic interactions play a larger role in suppressing branch formation in ethylene homopolymerizations, entropic effects appear to play an important role in modulating ethylene–hexene copolymerizations. This result is reminiscent of a recent study by Ehm and co-workers, who studied the relative contributions of enthalpy and entropy to ethylene/α-olefin copolymerizations using group 4 olefin polymerization catalysts.[75]

Conclusions

In sum, we performed a multifaceted computational and experimental study combining DFT, EPR measurements, and magnetic susceptibility measurements to better understand the mechanisms underlying polyolefin microstructure modulation by a redox-switchable Ni(II) α-diimine catalyst. Though the structure and electronic nature of the native catalyst are well known in the literature, that of the reduced form had yet to be fully described.

Our studies revealed that the geometry around the Ni center of precatalyst $\mathbf{1}_{\mathbf{red}}$ remains tetrahedral upon reduction, but that the oxidation state of Ni decreases from +2 to +1. However, upon methylation and activation, the geometries of the native and reduced complexes transition from tetrahedral to square-planar, and the added electron of precatalyst $\mathbf{A1}_{\mathbf{red}}$ transfers from the Ni center to the dipp-BIAN ligand, reverting the oxidation state of Ni in the reduced complex from +1 to +2. Though the added electron is primarily concentrated on the organic ligand framework, the small fraction of excess electron density at the metal center weakens the binding of ethylene to the reduced active species. It also compromises the favorable β-agostic interaction between the branched alkyl ligand and the Ni center in the reaction intermediates of the reduced catalyst species $\mathbf{A1}_{\mathbf{red}}$. Due to the weakening of this β-agostic interaction, which is important for chain-walking and branch formation, selectivity is dictated by steric repulsion between the alkyl ligand and the dipp-BIAN ligand on the reduced intermediate complexes, thereby driving formation of a more linear polymer chain.

Our results also show that the decreased uptake of hexene in ethylene–hexene copolymerizations using reduced catalyst $\mathbf{A1}_{\mathbf{red}}$ primarily results from a greater entropic penalty of binding a longer-chain alkene to the Ni center of the reduced reaction intermediates. We hope that the insights into the individual roles of steric, electronic, and entropic effects described here will inform the development of future generations of redox-switchable olefin polymerization catalysts and enable new methods for tuning polyolefin microstructures.

Conflicts of interest

There are no conflicts to declare.

Acknowledgements

RCC, JLK and SR acknowledge the University of Tennessee for financial support of this research. WCA and BKL thank the Army Research Office for their financial support under contract no. W911NF-14-1-0138. The computational work was performed on the Advanced Computing Facility (ACF) and Newton high-performance computing clusters located at the University of Tennessee, Knoxville.

References

1 S. D. Ittel, L. K. Johnson and M. Brookhart, *Chem. Rev.*, 2000, **100**, 1169–1204.
2 L. K. Johnson, C. M. Killian and M. Brookhart, *J. Am. Chem. Soc.*, 1995, **117**, 6414–6415.
3 V. C. Gibson and S. K. Spitzmesser, *Chem. Rev.*, 2003, **103**, 283–316.
4 H. Makio, H. Terao, A. Iwashita and T. Fujita, *Chem. Rev.*, 2011, **111**, 2363–2449.
5 D. J. Walsh, M. G. Hyatt, S. A. Miller and D. Guironnet, *ACS Catal.*, 2019, **9**, 11153–11188.
6 F. Wang and C. Chen, *Polym. Chem.*, 2019, **10**, 2354–2369.
7 L. Guo, S. Dai, X. Sui and C. Chen, *ACS Catal.*, 2016, **6**, 428–441.
8 Z. Chen and M. Brookhart, *Acc. Chem. Res.*, 2018, **51**, 1831–1839.
9 M. G. Hyatt and D. Guironnet, *ACS Catal.*, 2017, **7**, 5717–5720.
10 I. E. Soshnikov, K. P. Bryliakov, A. A. Antonov, W.-H. Sun and E. P. Talsi, *Dalton Trans.*, 2019, **48**, 7974–7984.
11 I. M. Lorkovic, R. R. Duff and M. S. Wrighton, *J. Am. Chem. Soc.*, 1995, **117**, 3617–3618.
12 C. K. A. Gregson, V. C. Gibson, N. J. Long, E. L. Marshall, P. J. Oxford and A. J. P. White, *J. Am. Chem. Soc.*, 2006, **128**, 7410–7411.
13 M. Zhao and C. Chen, *ACS Catal.*, 2017, **7**, 7490–7494.
14 M. Chen, B. Yang and C. Chen, *Angew. Chem.*, 2015, **127**, 15740–15744.
15 C. Chen, *ACS Catal.*, 2018, **8**, 5506–5514.
16 A. J. Teator, D. N. Lastovickova and C. W. Bielawski, *Chem. Rev.*, 2016, **116**, 1969–1992.
17 V. Lyaskovskyy and B. de Bruin, *ACS Catal.*, 2012, **2**, 270–279.
18 F. A. Leibfarth, K. M. Mattson, B. P. Fors, H. A. Collins and C. J. Hawker, *Angew. Chem., Int. Ed.*, 2013, **52**, 199–210.
19 J. M. Kaiser and B. K. Long, *Coord. Chem. Rev.*, 2018, **372**, 141–152.
20 J. M. Kaiser, W. C. Anderson and B. K. Long, *Polym. Chem.*, 2018, **9**, 1567–1570.
21 W. C. Anderson, J. L. Rhinehart, A. G. Tennyson and B. K. Long, *J. Am. Chem. Soc.*, 2016, **138**, 774–777.
22 L. A. Brown, J. L. Rhinehart and B. K. Long, *ACS Catal.*, 2015, **5**, 6057–6060.

23 W. C. Anderson, S. H. Park, L. A. Brown, J. M. Kaiser and B. K. Long, *Inorg. Chem. Front.*, 2017, **4**, 1108–1112.
24 W. C. Anderson and B. K. Long, *ACS Macro Lett.*, 2016, **5**, 1029–1033.
25 I. L. Fedushkin, A. A. Skatova, V. A. Chudakova and G. K. Fukin, *Angew. Chem., Int. Ed.*, 2003, **42**, 3294–3298.
26 I. L. Fedushkin, A. A. Skatova, V. A. Chudakova, V. K. Cherkasov, G. K. Fukin and M. A. Lopatin, *Eur. J. Inorg. Chem.*, 2004, **2004**, 388–393.
27 W. Gao, L. Xin, Z. Hao, G. Li, J.-H. Su, L. Zhou and Y. Mu, *Chem. Commun.*, 2015, **51**, 7004–7007.
28 I. L. Fedushkin, N. M. Khvoinova, A. A. Skatova and G. K. Fukin, *Angew. Chem., Int. Ed.*, 2003, **42**, 5223–5226.
29 I. L. Fedushkin, A. A. Skatova, S. Y. Ketkov, O. V. Eremenko, A. V. Piskunov and G. K. Fukin, *Angew. Chem., Int. Ed.*, 2007, **46**, 4302–4305.
30 I. L. Fedushkin, A. N. Lukoyanov, S. Y. Ketkov, M. Hummert and H. Schumann, *Chem. – Eur. J.*, 2007, **13**, 7050–7056.
31 H. Schumann, M. Hummert, A. N. Lukoyanov and I. L. Fedushkin, *Organometallics*, 2005, **24**, 3891–3896.
32 M. M. Khusniyarov, K. Harms, O. Burghaus and J. Sundermeyer, *Eur. J. Inorg. Chem.*, 2006, **2006**, 2985–2996.
33 Z. Guan, *Chem. – Asian J.*, 2010, **5**, 1058–1070.
34 L. Deng, P. Margl and T. Ziegler, *J. Am. Chem. Soc.*, 1997, **119**, 1094–1100.
35 L. Deng, T. K. Woo, L. Cavallo, P. M. Margl and T. Ziegler, *J. Am. Chem. Soc.*, 1997, **119**, 6177–6186.
36 T. K. Woo, P. E. Blöchl and T. Ziegler, *J. Phys. Chem. A*, 2000, **104**, 121–129.
37 T. K. Woo and T. Ziegler, *J. Organomet. Chem.*, 1999, **591**, 204–213.
38 D. A. C. Ferreira, S. M. P. Meneghetti, M. D. O. Neto, W. R. Rocha and M. R. Meneghetti, *J. Braz. Chem. Soc.*, 2011, **22**, 428–436.
39 S. Ibáñez, M. Poyatos, L. N. Dawe, D. Gusev and E. Peris, *Organometallics*, 2016, **35**, 2747–2758.
40 S. M. Quan, J. Wei and P. L. Diaconescu, *Organometallics*, 2017, **36**, 4451–4457.
41 S. Klenk, S. Rupf, L. Suntrup, M. van der Meer and B. Sarkar, *Organometallics*, 2017, **36**, 2026–2035.
42 D. N. Lastovickova, A. J. Teator, H. Shao, P. Liu and C. W. Bielawski, *Inorg. Chem. Front.*, 2017, **4**, 1525–1532.
43 A. Feyrer, M. K. Armbruster, K. Fink and F. Breher, *Chem. – Eur. J.*, 2017, **23**, 7402–7408.
44 D. F. Evans, *J. Chem. Soc.*, 1959, 2003–2005, DOI: 10.1039/JR9590002003.
45 *Gaussian 09, Revision D.01*, M. J. Frisch, G. W. Trucks, H. B. Schlegel, G. E. Scuseria, M. A. Robb, J. R. Cheeseman, G. Scalmani, V. Barone, B. Mennucci, G. A. Petersson, H. Nakatsuji, M. Caricato, X. Li, H. P. Hratchian, A. F. Izmaylov, J. Bloino, G. Zheng, J. L. Sonnenberg, M. Hada, M. Ehara, K. Toyota, R. Fukuda, J. Hasegawa, M. Ishida, T. Nakajima, Y. Honda, O. Kitao, H. Nakai, T. Vreven, J. A. Montgomery, Jr., J. E. Peralta, F. Ogliaro, M. Bearpark, J. J. Heyd, E. Brothers, K. N. Kudin, V. N. Staroverov, T. Keith, R. Kobayashi, J. Normand, K. Raghavachari, A. Rendell, J. C. Burant, S. S. Iyengar, J. Tomasi, M. Cossi, N. Rega, J. M. Millam, M. Klene, J. E. Knox, J. B. Cross, V. Bakken, C. Adamo, J. Jaramillo, R. Gomperts, R. E. Stratmann, O. Yazyev, A. J. Austin, R. Cammi, C. Pomelli, J. W. Ochterski, R. L. Martin, K. Morokuma, V. G. Zakrzewski, G. A. Voth, P. Salvador, J. J. Dannenberg, S. Dapprich, A. D. Daniels, O. Farkas, J. B. Foresman, J. V. Ortiz, J. Cioslowski and D. J. Fox, Gaussian, Inc., Wallingford CT, 2013.
46 J. Tao, J. P. Perdew, V. N. Staroverov and G. E. Scuseria, *Phys. Rev. Lett.*, 2003, **91**, 146401.
47 T. H. Dunning Jr., *J. Chem. Phys.*, 1989, **90**, 1007–1023.
48 R. A. Kendall, T. H. Dunning Jr. and R. J. Harrison, *J. Chem. Phys.*, 1992, **96**, 6796–6806.
49 G. I. Csonka, J. P. Perdew and A. Ruzsinszky, *J. Chem. Theory Comput.*, 2010, **6**, 3688–3703.
50 C. J. Cramer and D. G. Truhlar, *Phys. Chem. Chem. Phys.*, 2009, **11**, 10757–10816.
51 M. Bühl and H. Kabrede, *J. Chem. Theory Comput.*, 2006, **2**, 1282–1290.
52 T. Weymuth, E. P. A. Couzijn, P. Chen and M. Reiher, *J. Chem. Theory Comput.*, 2014, **10**, 3092–3103.
53 M. Bühl, C. Reimann, D. A. Pantazis, T. Bredow and F. Neese, *J. Chem. Theory Comput.*, 2008, **4**, 1449–1459.
54 F. Furche and J. P. Perdew, *J. Chem. Phys.*, 2006, **124**, 044103.
55 J. N. Harvey, *Annu. Rep. Prog. Chem., Sect. C: Phys. Chem.*, 2006, **102**, 203–226.
56 F. Neese, *Coord. Chem. Rev.*, 2009, **253**, 526–563.
57 R. Peverati and G. Truhlar Donald, *Philos. Trans. R. Soc., A*, 2014, **372**, 20120476.
58 D. Rappoport, N. R. Crawford, F. Furche and K. Burke, in *Encyclopedia of Inorganic and Bioinorganic Chemistry*, 2011, DOI: 10.1002/9781119951438.eibc0380.
59 N. E. Schultz, Y. Zhao and D. G. Truhlar, *J. Phys. Chem. A*, 2005, **109**, 11127–11143.
60 V. N. Staroverov, G. E. Scuseria, J. Tao and J. P. Perdew, *J. Chem. Phys.*, 2003, **119**, 12129–12137.
61 C. J. Ziegler, K. Chanawanno, A. Hasheminsasab, Y. V. Zatsikha, E. Maligaspe and V. N. Nemykin, *Inorg. Chem.*, 2014, **53**, 4751–4755.
62 Y. Zhou, K. T. Ngo, B. Zhang, Y. Feng and J. Rochford, *Organometallics*, 2014, **33**, 7078–7090.
63 S. Kossmann, B. Kirchner and F. Neese, *Mol. Phys.*, 2007, **105**, 2049–2071.
64 S. Grimme, J. Antony, S. Ehrlich and H. Krieg, *J. Chem. Phys.*, 2010, **132**, 154104.
65 S. Grimme, S. Ehrlich and L. Goerigk, *J. Comput. Chem.*, 2011, **32**, 1456–1465.
66 J. Tomasi, B. Mennucci and R. Cammi, *Chem. Rev.*, 2005, **105**, 2999–3094.
67 I. E. Soshnikov, N. V. Semikolenova, K. P. Bryliakov, A. A. Antonov, V. A. Zakharov and E. P. Talsi, *Dalton Trans.*, 2018, **47**, 4968–4974.
68 I. E. Soshnikov, N. V. Semikolenova, K. P. Bryliakov, A. A. Antonov, W.-H. Sun and E. P. Talsi, *J. Organomet. Chem.*, 2019, **880**, 267–271.
69 I. L. Fedushkin, A. A. Skatova, A. N. Lukoyanov, N. M. Khvoinova, A. V. Piskunov, A. S. Nikipelov, G. K. Fukin, K. A.

Lysenko, E. Irran and H. Schumann, *Dalton Trans.*, 2009, **24**, 4689–4694.

70 D. Meinhard, P. Reuter and B. Rieger, *Organometallics*, 2007, **26**, 751–754.

71 V. V. Khrizanforova, R. R. Fayzullin, V. I. Morozov, I. F. Gilmutdinov, A. N. Lukoyanov, O. N. Kataeva, T. P. Gerasimova, S. A. Katsyuba, I. L. Fedushkin, K. A. Lyssenko and Y. H. Budnikova, *Chem. – Asian J.*, 2019, **14**, 2979–2987.

72 B. K. Bahuleyan, G. W. Son, D.-W. Park, C.-S. Ha and I. Kim, *J. Polym. Sci., Part A: Polym. Chem.*, 2008, **46**, 1066–1082.

73 M. Brookhart, M. L. H. Green and G. Parkin, *Proc. Natl. Acad. Sci. U. S. A.*, 2007, **104**, 6908.

74 A. E. Reed, R. B. Weinstock and F. Weinhold, *J. Chem. Phys.*, 1985, **83**, 735–746.

75 F. Zaccaria, C. Ehm, P. H. M. Budzelaar and V. Busico, *ACS Catal.*, 2017, **7**, 1512–1519.